Determining the Spectral Energy Distribution of two Features of NGC 5128

Guy Leckenby

Supervisor: Christian Wolf

PhB Advanced Studies Course, Research School of Astronomy & Astrophysics
The Australian National University, Canberra, ACT 2611, Australia

June 5, 2016

Abstract

Accurate spectral energy distributions (SED) are required for structural analysis of galactic evolution. In this report, the SEDs of two features of NGC 5128 are determined from deep field images produced by the SkyMapper telescope. NGC 5128 is particularly powerful in this regard because its proximity allows for high resolution images demonstrating features not visible in other galaxies. The images were PSF homogenised and then the foreground objects were subtracted to reveal the underlying galaxy. Unfortunately this object masking removed the features being analysed and hence two different methods were developed to produce flux densities for the objects. These density images were then used to produce the required SEDs. The process demonstrated in this report will be useful for further feature analysis.

I. Introduction

On scales of $< 100\,Mpc$, which correspond to the largest known matter aggregates, the density of galaxies varies by four orders of magnitude from intergalactic voids to the cores of rich clusters (Boselli & Gavazzi 2006). It has long been known that the Hubble type and local density are related (Hubble & Humason 1931), in particular elliptical and lenticular galaxies are found near higher concentrations whilst spirals dominate sparsely populated regions. This morphological separation has prompted an ongoing investigation into the environmental effects on galaxies in an attempt to provide a physically motivated explanation for the observed segregation.

Of primary concern is the environmental effects on star formation rates and stellar populations which directly influence the observed spectral energy distributions. In particular, the processes determining the evolution of galaxies is largely undetermined. This is a result of the extremely complex interactions between dark matter halos, dust and gaseous components, star populations in the disc and bulge regions, and the interactions of supermassive black holes. One method of confining the evolutionary track of galaxies is to examine high redshift examples to sample galaxies during their earliest formation periods which has met with much success in constraining global star formation rates and black hole accretion (Croom et al. 2011). However detailed evolutionary dynamics requires specific spectral energy distributions which are not attainable at these high redshifts (Boselli & Gavazzi 2006). Hence nearby galaxy clusters are still important for determining galactic evolution.

In particular nearby galaxy clusters like Virgo, Coma and Abell 1367 allow for a variety of electromagnetic wavelengths to be studied due to their proximity. Furthermore, on top of being the some of the best studied systems in the sky, these cluster provide a range of evolutionary stages to assess intergalactic effects like ram pressure stripping and merging on star formation (Boselli & Gavazzi 2006). Rest frame ultraviolet and Hα emission are good tracers of ongoing star formation, optical bands provide morphological information, near infrared traces ageing populations whilst mid and far infrared follows dust, and the 21 cm line identifies primordial gas movements. This variety of characteristic features is only observable with low redshifts and thus nearby galaxies are particular powerful in evolutionary studies.

One particular nearby galaxy that provides a particularly complex laboratory for several aspects of evolutionary dynamics is NGC 5128. Due to its proximity, resolution of internal features in several bands is possible which provides enormous information on stellar populations and dynamics. This report will investigate NGC 5128 and it's contribution to understanding galactic evolution.

II. NGC 5128 (Centaurus A)

The giant elliptical galaxy NGC 5128, often conflated with it's central radio source named Centaurus A, is one of the closest giant ellipticals and provides a wealth of information on stellar populations and evolution due to the resolution attainable. The distance to NGC 5128 has recently been narrowed down to $d = 3.82 \pm 0.09\,Mpc$ by a comparison of five stellar distance indicators (Harris et al. 2010). This proximity of NGC 5128 allows us to identify hundreds of globular clusters and planetary nebula (Harris, 2010) which provide details on the star formation history and populations of the system.
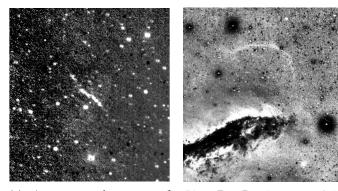
NGC 5128 is an even more interesting object as it is suspected to be the result of a merging event between a small gas rich spiral galaxy with a larger elliptical galaxy within the last Gyr (Brookes et al. 2013). This conclusion is a result of observation of optical shells which are a natural effect of such merging activity (Malin et al. 1983). The dust lane is presumed to have been generated in the same event and is located inside the halo giving rise to high star formation activity surrounding and within the disk (Israel 1998). One of the objects studied in this report is suspected to be the debris of a tidally disrupted dwarf galaxy involved in the merger (Peng et al. 2002). These complex structures and filaments observable provide very good tests for our understanding of galactic evolution.

Figure 1: A g-band image of NGC 5128 showing the bright, circular central bulge crossed by a complex dust lane which points directly to previous merging activity.

In addition to this, Centaurus A is a Fanaroff-Riley Class I radio galaxy and offers one of the best opportunities to observe energy transfer from an active galactic nucleus (AGN) to the intergalactic medium via relativistic jets (Mould et al. 2000). These jets are believed to be inducing star formation activity in the northeast halo regions (Fasset & Graham 2000) which is the other object of study for this report. Whilst Centaurus A demonstrates many other interesting features including large elongated radio lobes (Israel 1998), this report will focus on the inner optical knots observable.

As indicated above, this report will focus on two features of this system, the shock induced star formation knots and the debris of the tidally disrupted dwarf stream, both seen in Figure 2. By ascertaining spectral energy distributions of these two features, it is hoped the star formation history and

other stellar population mechanics will be analysed to provide information on the dynamics of the features which will inform our understanding of the evolution of NGC 5128 itself.

III. DEEP FIELD IMAGES

The images used in this investigation were deep field images of NGC 5128 taken by the SkyMapper telescope at Siding Spring Observatory. The telescope is a 1.35 m wide-angle optical telescope and uses 32 individual 4096×2048 pixel CCDs which cover a $2.373° \times 2.395°$ field of view (Granlund et al. 2006). SkyMapper's primary purpose is to produce a survey of the southern sky, inspired to some extent by the Sloan Digital Sky Survey (SDSS). It observes from 340 nm - 1 micron wavelengths with its unique filter set being primarily designed for stellar photometry to discriminate metallicity, effective temperature and effective gravity in stars (Bessel et al. 2011). In particular the SDSS filters have been modified with u and g being separated for a narrow violet v filter to be inserted, as demonstrated in the noramalised pass band diagrams in Figure 3; the specific details of which are provided in Table 1.

The original images were taken throughout May of 2014. Each exposure was 5 minutes long and between 22 and 105 exposures were taken for each frame. To remove artefacts, the images were dithered and rotated 0, 15 30, 45, 60, 75, 90 or 270 degrees and then translated between ± 0.167 degrees to ensure each pixel in the final image was the result of at least 2 data points although generally more were used (Golding 2015). Each image was processed via coaddition of frames using SWarp, the full process including background normalisation is described by Golding (2015). The resulting full images are deep field images composed of up to 15 data points per pixel

Table 1: The SkyMapper filter set specifications.

Filter	Center	FWHM	50% Cut-on Edge	50% Cut-off Edge
u	350	55	312	367
v	384	31	365	396
g	510	146	417	663
r	617	148	555	703
i	779	140	703	843
z	916	~116	852	Detector Cut-off

(a) A $v - g$ colour map of the shock induced star formation knots.

(b) A $B - R$ colour map of the tidally disrupted dwarf as imaged by Peng et al. (2002).

Figure 2: The two features of NGC 5128 studied in this report.

Figure 3: The normalised Skymapper pass band response functions for the $uvgriz$ filter set.

Table 2: Average PSF parameters and the results of the PSF homogenisation.

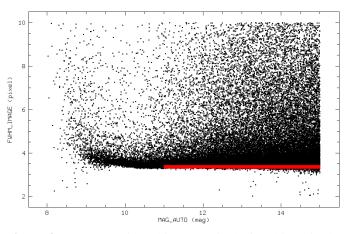| Band	FWHM (px)	Elong.	θ_{sky} (°)	$1^{st}\ \sigma$	1st FWHM (px)	$2^{nd}\ \sigma$	2nd FWHM (px)
u	3.3823	1.0554	59.306	-	-	-	-
v	2.9755	1.0414	76.066	0.6829	3.4927	0.6120	3.3893
g	2.6884	1.0322	−15.659	0.8716	3.5733	0.7589	3.3806
r	1.9150	1.0742	−89.069	1.1839	3.5856	1.0900	3.3899
i	2.3405	1.0873	64.581	1.0369	3.5619	0.9450	3.3711
z	1.8316	1.0708	82.796	1.2075	3.5172	-	-
Hα	1.8084	1.0965	−84.163	1.2138	3.5131	-	-

which provide high resolution details of NGC 5128's structure and surrounding objects. The images used in this report are for seven pass bands, u, v, g, r, i, z and $H\alpha$.

IV. PSF Homogenisation

Many interesting astrophysical conclusions about the structure and composition of stellar populations can only be determined from colour ratio images. However to be able to compute these ratio images, all the frames must have the same point spread function (PSF) otherwise the same object will have differing angular sizes over the images. The PSF of an optical system is the response function to a point source. Stars and quasars approximate points sources very well in astronomical applications and hence to determine the PSF of an image, the stellar field needs to be analysed. For ground based telescopes, the PSF is dominated by atmospheric turbulence which varies significantly for each exposure (Énard et al 1996). The actual function is highly complex as it depends on the exact thermodynamic movement of the atmosphere above as well as the diffraction of the telescope however it is reasonably well approximated by a Gaussian distribution (Énard et al 1996). Hence to determine the PSF of each deep field image, the stellar field needs to be analysed.

Obviously their are many more objects than foreground stars in each image, especially since they are deep field. These objects can mostly be removed by putting constraints on the type of objects used to calculate the average PSF of each image. However even by eliminating non-stellar components from the process, the parameters of the PSF have a natural scatter distribution. This is a result of the fact that over SkyMapper's field of view, the turbulence of the atmosphere varies and thus the PSF will change continuously over the image. Attempting to account for this intrinsic variation of the atmosphere is impossible and thus the PSF of the image is taken as the average of the stellar objects.
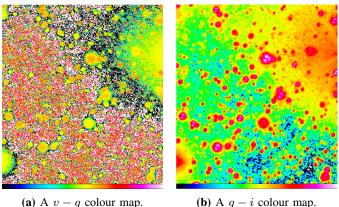
To do this, an appropriate subpopulation of stellar objects needed to be identified that was representative of the scatter around the mean. To acheive this, Source Extractor was used to produce a FITS catalogue of objects in each image. Faint objects (generally $m > 15$) were discarded due to the pixel limit; a smooth PSF cannot accurately be determined from an object spanning only a few pixels. Bright objects (generally $m < 10$) were discarded as these objects had reached the saturation level of the CCD and thus demonstrated a flat topped distribution rather than the PSF resulting in an artificial increase of the full-width half-maximum (FWHM). Finally galaxies generate objects with large FWHM and elongation

(the elongation being a measure of the ellipticity; elong. $= \frac{a}{b}$ where a and b are the semi-major/minor axes). As seen in Figure 4, these galaxies generate a gradually reducing tail towards larger FWHM values that merges with the stellar population. To eliminate the galaxies, the selection was cropped for both FWHM and elongation plots until the scatter was approximately random and no drop off could be seen in the frame. This selection, plotted in red in Figure 4, could then give an accurate determination of the average PSF for the image.

Figure 4: FWHM against object magnitude for objects in the g-band image. The objects in red are those used to determine the PSF average.

Conducting this process of averaging over all of the provided images yielded the results of Table 2. The shorter wavelength bands have considerably broader PSF's which is expected as shorter wavelengths undergo more Rayleigh scattering through the atmosphere. Furthermore each PSF has a small ellipticity parametrised by the elongation and the orientation angle θ_{sky}. These parameters can then be used to homogenise the PSF's over all bands to allow ratio images to be computed.

To homogenise the PSF, each image must be convolved with a kernel such that the resulting PSF is homogenous across all the bands. The PSFs are approximately Gaussian and as the convolution of two Gaussians is a Gaussian (where the expected values add and the squares of the variances add), naturally the kernel will also be Gaussian (Weisstein n.d.). This convolution is generally two-dimensional to account for the ellipticity of the PSF however because the elongation in each band was less than 1.1, it was proposed that the PSFs could be approximated as circular thus vastly simplifying the convolution. In particular, the FWHM is related to the variance

(a) A $v - g$ colour map.   **(b)** A $g - i$ colour map.

Figure 5: Two cutouts of ratio images constructed from the PSF homogenised images.

by FWHM $= 2\sqrt{2\ln 2}\,\sigma$ such that the variance of the kernel can be calculated as

$$\sigma_{\text{ker}} = \sqrt{\left(\frac{\text{FWHM}_u}{2\sqrt{2\ln 2}}\right)^2 - \left(\frac{\text{FWHM}_x}{2\sqrt{2\ln 2}}\right)^2} \tag{1}$$

where x corresponds to the band being homogenised and u is the final PSF as the u band has the largest natural PSF. A Gaussian filter using the calculated kernel can then be used to homogenise the PSF for each band, in theory.

When the Gaussian filter (with kernel's derived as above) were applied to the images however, the resultant FWHM's observed were 0.1-0.2 pixels larger than expected. This is seen in the 1st FWHM column of Table 2. This discrepancy is presumed to result from the fact that the PSF's are not Gaussian and hence the squared variance cannot be added perfectly. Thus a second attempt was made by simply guessing and checking until PSFs within 0.01 of the u-band FWHM were found. Figure 5 shows two ratio images produced using the homogenised images. As evident, the $v-g$ colour map, where both frames had low elongations, looks much as expected. However in the $g-i$ colour map, some stars demonstrate a double peak which is a sign of the ellipticity of the PSFs not corresponding. Thus to get images with elongations greater than 1.8, elliptical convolutions would have to be considered. Given time constraints, it was decided that the u, v, g, r bands demonstrated the majority of the stellar features desired and hence the i, z and $H\alpha$ bands were disregarded. A more complete investigation would calculate the elliptical convolution enabling analysis of these bands.

V. OBJECT MASKING

To effectively study the galactic structure of NGC 5128 in the homogenised images, it was necessary to remove the foreground stars. Using Source Extractor to identify the objects, this should have been straightforward. Source Extractor can output some of the maps used during intermediate steps of processing, these are termed the *check-images*. One check-image is the objects frame which plots the flux of everything that Source Extractor has decided is an object. This is extremely useful as to remove the foreground stars, all that needs to be

done is to subtract the objects frame from the original image leaving the observed background, not just the background that Source Extractor predicts.

Unfortunately for the default settings, Source Extractor also detects the majority of the centre of NGC 5128 as an object and removes it as well. The detection threshold relative to the background can be altered by the parameter `back_size` which controls the pixel radius used when determining what qualifies as 'the background' and what could qualify as an
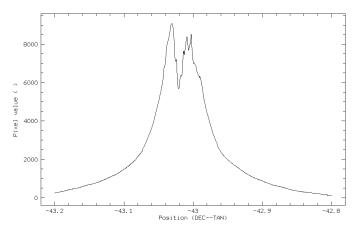

Figure 6: An averaged intensity plot for the right ascensions 201.3004 - 201.4395 corresponding to the centre of NGC 5128. The jagged peak is generated by the dust lane which obscures the central bulge.
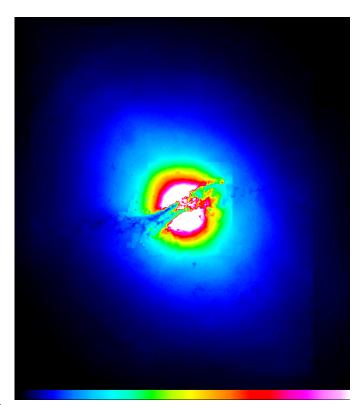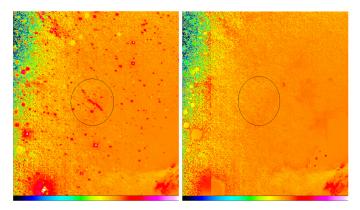

Figure 7: The masked g-band deep field image of NGC 5128. Square artefacts from changing `back_size` are visible around the centre and the right edge.

object. If the `back_size` is too large, then variations in the background will be ignored, if the `back_size` is too small, flux from some objects will be considered as part of the background. In the second case, this is desirable for the centre of NGC 5128 which is quite bright but extended. By using a smaller `back_size`, the parts of NGC 5128 included in the objects frame were limited to the highly variant flux around the dust lane which could be removed manually. However a low `back_size` includes some foreground stars that are quite noticeable in the halo of the galaxy. Thus a compromise of three different `back_size` values was used for different radii to produce the ideal image. Whilst this produced the optimal image in terms of minimising foreground stars and maximising structure maintained, it did introduce square artefacts in the image where the background estimation changes. This is seen in Figure 7 which is the resulting masked image in the g-band. Figure 6 is a plot of the averaged flux between the right ascensions of 201.3004 and 201.4395 and it shows clearly the smooth edges of the giant elliptical galaxy. The peak of the plot is jagged due to the dust lane which obscures the central bulge.
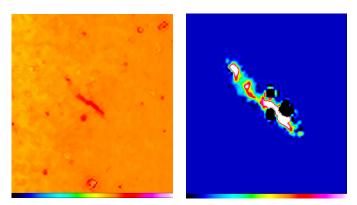
There is one major problem with this masking technique however. Of the two features to be studied in NGC 5128, the jet induced star formation knots are removed during the object subtraction. This seen in the comparison of the $v - g$ ratio images in Figure 8 which most clearly show the knots and then their disappearance after masking. This is problematic as the primary aim of the report was to measure the SED of the feature. Furthermore, it was not possible to simply remove this area from the object frame as there are foreground stars embedded in the feature that would dominate the SED. Hence an alternate method is required to separate the stars from the feature. This will be the focus of the next section.

Figure 8: The $v - g$ ratio image both before (left) and after object masking (right). Notably the feature of interest is also removed during the masking process.

VI. Feature Detection

To observe the SED of the knots without the embedded stars required a different approach to simply subtracting the detected objects from the original image. If the `back_size` is set to a very low value, then only very localised objects will be detected by Source Extractor. In particular, this means that
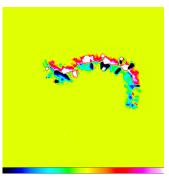

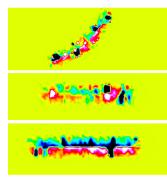**(a)** A $v - g$ colour map of the estimated background.

(b) The final flux image of the knots feature.

Figure 9: Two images from the process of producing the SED for the knots feature.

the *background check image* generated by Source Extractor will contain the flux signatures of any object appropriately diffuse whilst still removing the stars. Utilising this fact, the `back_size` was set slightly larger than the radii of the stars embedded in the knots such that when the background check image was produced, it contained the desired features but not the embedded stars. Source Extractor can also weight an image whilst determining the background and hence a binary mask was used to create a background estimate from which the knots were excluded. In particular by subtracting the weighted background estimate from the non-weighted background estimate, a flux density was produced that was solely attributed to any variations inside the weighted mask, that is the profile of the knots. This technique produced the image in Figure 9b. Note that because of the weighting, the weighted background estimate included some of the flux from the stars embedded. These 'holes' were set to zero as the negative flux should not contribute.

The question remains whether this technique works for the tidally disrupted dwarf which is much fainter across the galaxy.
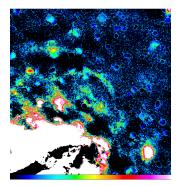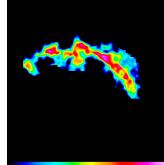

(a) A $v - g$ colour map of the tidal dwarf using the same technique as for the knots.

(b) Similar $v - g$ colour maps using the same technique on apparently random parts of the galaxy.

Figure 10: A comparison of the technique applied to the dwarf (a) and to three random patches of the galaxy (b). As evident, little difference is noticeable.

(a) The original image with the object (`bs=16`) and background (`bs=64`) frames subtracted.

(b) The final flux image of the tidally disrupted dwarf feature after smoothing.

Figure 11: Two images from the process of producing the SED for the tidal dwarf feature. The dwarf can be seen as the arc just above centre in (a).

This was addressed by comparing the images produced via the above technique with the same technique applied to apparently empty patches of the galaxy, as seen in Figure 10. The supposed random patches of galaxy show very similar flux profiles and in both cases the negative flux (the zero level is set at yellow) is almost equivalent to the positive flux. Thus it is clear that the natural uncertainty associated with the technique smothers the flux coming from the feature.

Thus a different technique was employed to ascertain a flux image of the tidally disrupted dwarf. An object frame was taken using a `back_size` of 16 and a background frame taken using a `back_size` of 64. Both were subtracted from the original image leaving only objects that were considered too faint for a `back_size` of 16 but too bright for a `back_size` of 64. This image is seen in Figure 11a where the shape of the tidally disrupted dwarf can clearly be seen. By applying a Gaussian filter and masking the surrounding noise, a flux image (Figure 11b) was produced that could be analysed.

VII. THE SPECTRAL ENERGY DISTRIBUTION

Using the above techniques images, of the physical fluxes attributable to each feature can be produced as seen in Figure 9b and 11b. These flux measurements can then be converted to absolute magnitudes by comparing the observed flux with objects of known brightness in the field. In particular five stars (of which one was discarded as an outlier) in uncrowded fields whose absolute magnitude was known were used to determine the absolute magnitudes of the features in each band, the results of which are provided in Table 3.

Table 3: The spectral energy distribution for both features quoted in absolute magnitudes.

Band	Knots (mag)	σ_{knots} (mag)	Dwarf (mag)	σ_{dwarf} (mag)
u	17.68673	0.011041	17.61554	0.011041
v	17.26069	0.018823	17.42856	0.018823
g	17.12196	0.003469	16.52237	0.003004
r	17.20987	0.016944	16.14795	0.016944

Uncertainties in the SED

Three sources of uncertainty were considered when determining the SED of the two features. The first was that the flux measurements of the feature induced Poissonian noise from the observation. Because both objects are faint compared to the background (and the background was subtracted to isolate the feature), the Poissonian uncertainty in each flux measurement was sourced from the background area of the weighting mask which was considerably larger than the Poissonian uncertainty of the feature flux measurement. This uncertainty was then propagated by

$$\sigma_{\text{mag}} = 0.434\sqrt{\frac{1}{F_\text{s}} + \frac{F_{\text{bkg}}}{F_{\text{feat}}^2}} \tag{2}$$

to give the uncertainty in the absolute magnitude where F_s is the flux from the calibration star, F_{bkg} is the flux from the background and F_{feat} is the flux from the feature itself.

The Poissonian uncertainty was consistently smaller than the zero-point uncertainty however. This was determined by the standard deviation from the mean of the set of stars used to determine the average absolute magnitude. In particular

$$\sigma_{\text{zp}} = \sqrt{\frac{\sum_i^n (\mu - x_i)^2}{n}} \tag{3}$$

where μ is the mean, n is the number of stars considered and x_i is the result for the ith star. The zero point error calculated this way are the errors presented in Table 3 and are very small (on average 0.07%). This indicates that the Poissonian error is very small and that the zero-point determination is very good.

Both these sources of uncertainty however assume that the flux isolated by the techniques described in Section VI are perfect which is obviously not the case. For example hole's generated by the stars will have masked some of the flux from the knots and in both cases, the wings of stellar PSF's will not have necessarily been filtered and thus will contribute noise to the image. To measure this uncertainty, it is suggested that the same technique be applied to a blank section of the galaxy to determine the influence of the galaxy's microstructures. This was trialled for the technique used on the knots in the g-band and yielded an uncertainty of 2.67% in the measured flux value. As the Poissonian uncertainty corresponded to approximately 1% uncertainty in the flux value and the zero-point error was 2-4 magnitudes larger than the Poissonian error, it follows that error in the technique roughly equivalent to the zero-point error. Note that due to time constraints, only the above limited heuristic handling could be afforded. A more in depth investigation could better quantify the methodological error.

VIII. FUTURE WORK

This report has demonstrated two possible methods for determining the spectral energy distributions of features in deep field galactic imaging. This is however only a taste for the scope of progress in this area. In particular more work could be conducted on quantifying which of the two methods presented is more accurate. In particular, this would involve refining each method to be less subjective, that is remove the user choice of feature masking and develop a system with the

same control but more precision. Furthermore quantifying the methodological error is crucial in determining which method is superior and placing more realistic bounds on the observed uncertainty.

The band range of the SED is currently limited to those with appropriately circular PSF's. By developing an elliptical PSF homogenisation technique, the calculated SED could be expanded to the higher wavelength bands and $H\alpha$. This would could provide more detailed information on the older stellar population of features and the ongoing star formation rate. Furthermore, an elliptical PSF homogenisation would increase the accuracy of the shorter wavelength bands as well.

Finally with a SED of the features, the evolutionary structure could be investigated. Throughout the report, $v - g$ colour maps (Figures 2a & 9a) have suggested that the shock induced star formation knots contain a younger stellar population. This is in line with the expected jet induced theories and $H\alpha$ image could further shed light on the structure of these knots. This is true also for the tidally disrupted dwarf (Figure 2b) although it is very difficult to see in colour maps without contrast enhancement. This suggests tidal star formation triggered during the infall whilst merging with NGC 5128 that has since been quenched (Peng et al. 2002).

As star formation history is the primary driver of stellar population structure and a further avenue would be to use the SLUG stellar synthesis package to predict possible star formation histories of the two features. This would provide bounds on the possible mechanics behind the two features. Not only would this be mechanically interesting in terms of the structure of NGC 5128 itself, this work could provide a powerful example for the application of stellar population modelling in determination of other physical structures as well.

IX. CONCLUSION

In this report, the necessity of good photometric data for determining the structure of galaxies has been discussed. To demonstrate this, the giant elliptical galaxy NGC 5128 was considered due to it's proximity to the Milky Way allowing high resolution observation of features that would not be visible in other galaxies. Two of the these features, the shock induced star formation knots in the northeast halo and the tidally disrupted dwarf first discovered by Peng et al. (2002), were elected for investigation. The images used were deep field images from SkyMapper taken in seven bands and refined by coaddition. These images were subjected to a PSF homogenisation process in order to generate ratio images. Ultimately i, z and $H\alpha$ were discarded during this process due to their high ellipticity. The images were then processed by removing the foreground stars to produce smooth picture of the galaxy beneath, albeit with square artefacts due to alternating `back_size` values. However it was found that this process, whilst retaining the broad features, removed the features of interest. Hence the Source Extractor background check image was used to create a profile of the jet induced knots. This was determined not to work for the tidally disrupted dwarf so instead, a raw flux profile was extracted from the residuals of the original image after object and background subtraction although this increased the

associated noise. Thus a physical spectral energy distribution was determined. Both features were determined to have a young stellar population although further investigation using stellar synthesis software was suggested for a more thorough investigation.

REFERENCES

Bessell, M., Bloxham, G., Schmidt, B., Keller, S., Tisserand, P., & Francis, P., 2011, 'SkyMapper Filter Set: Design and Fabrication of Large-Scale Optical Filters,' *Publications of the Astronomical Society of the Pacific,* 123:789-98.

Boselli, A. & Gavazzi, G., 2006, 'Environmental Effects on Late-Type Galaxies in Nearby Clusters,' *Publications of the Astronomical Society of the Pacific,* 118:517-59.

Brookes, M., Keene, J., Stern, D., Lawrence, C., & Werner, M., 2013, 'Spitzer Observations of the Dusty Warped Disk of Centaurus A,' https://arxiv.org/pdf/astro-ph/0601135v1.pdf.

Croom, S., Lawrence, J., Bland-Hawthorn, J., Bryant, J., Fogarty, L., Richards, S., Goodwin, M., Farrell, T., Mixiarski, S., Heald, R., Jones, H., Lee, S., Colless, M., Brough, S., Hopkins, A., Bauer, A., Birhcall, M., Ellis, S., Horton, A., Leon-Saval, S., Lewis, G., López-Sánchez, Á., Min, S., Trinh, C., & Trowland, H., 2011, 'The Sydney-AAO Multi-object Integral field spectrograph (SAMI),' *Monthly Notices of the Royal Astronomical Society.*

Énard, D., Maréchal, A., & Espiard, J., 1996, 'Progress in ground-based optical telescopes,' *Progress Reports in Physics,* 59:601-56.

Fasset, C. & Graham, J., 2000, 'Age, Evolution, and Dispersion of the Loose Groups of Blue Stars in the Northeast Radio Lobe of Centaurus A,' *The Astrophysical Journal,* 538:594-607.

Golding, J., 2015, 'Centaurus A data from SkyMapper: The coaddition process of SkyMapper data and an investigation of colour features in the Centaurus A field,' *ASTR3005 Project Report.*

Granlund, A., Conroy, P., Keller, S., Oates, A., Schmidt, B., Waterson, M., Kowald, E., & Dawson, M., 2006, 'A large-format imager for the SkyMapper Survey Telescope,' *SPIE Proceedings: Ground-based and Airborne Instrumentation for Astronomy,* vol. 6269.

Harris, G., 2010, 'NGC 5128: The Giant Beneath,' *Publications of the Astronomical Society of Australia,* 27:475-81.

Harris, G., Rejkuba, M., & Harris, W., 2010, 'The Distance to NGC 5128 (Centaurus A),' *Publications of the Astronomical Society of Australia,* 27:457-62.

Hubble, E. & Humason, M., 1931, 'The Velocity-Distance Relation among Extra-Galactic Nebulae,' *The Astrophysical Journal,* 74:43-80.

Israel, F., 1998, 'Centaurus A - NGC 5128,' *The Astronomy and Astrophysics Review,* 8:237-78.

Malin, D., Quinn, P., & Graham, J., 1983, 'Shell Structure in NGC 5128,' *The Astrophysical Journal,* 272:L5-L7.

Mould, J., Ridgewell, A., Gallagher, J., Bessel, M., Keller, S., Clazetti, D., Clarke, J., Trauger, J., Grillmair, C., Ballester, G., Burrow, C., Kirst, J., Crisp, D., Evans, R., Griffiths, R., Hester, J., Hossel, J., Holtsman, J., Scowen, P., Stapelfeldt, K., Sahai, R., Watson, A., & Meadows, V., 2000, 'Jet-Induced Star Formation in Centaurus A,' *The Astrophysical Journal,* 536:266-76.

Peng, E., Ford, H., Freeman, K., & White, R., 2002, 'A Young Tidal Blue Stream in NGC 5128,' *The Astrophysical Journal,* 124:3144-56.

Weisstein, E. n.d. "Convolution." From MathWorld - A Wolfram Web Resource.